Available online at www.sciencedirect.com

jmr&t Journal of Materials Research and Technology

journal homepage: www.elsevier.com/locate/jmrt

Original Article

A high Fe-containing AlSi12 alloy fabricated by laser powder bed fusion

Xinhai Ai [a], Jianying Wang [a], Tao Wen [a], Feipeng Yang [a], Xixi Dong [b,**], Hailin Yang [a,*], Shouxun Ji [b]

[a] State Key Laboratory of Powder Metallurgy, Central South University, Changsha 410083, China
[b] Brunel Centre for Advanced Solidification Technology (BCAST), Brunel University London, Uxbridge, Middlesex, UB8 3PH, United Kingdom

ARTICLE INFO

Article history:
Received 28 February 2022
Accepted 2 April 2022
Available online 27 April 2022

Keywords:
Aluminum alloy
Additive manufacturing
Microstructure
Mechanical properties
Iron phase
Strengthening mechanisms

ABSTRACT

The high Fe-containing AlSi12 alloy was processed by additive manufacturing of laser powder bed fusion (LPBF) to understand the features of microstructures and mechanical properties under as-fabricated condition. The Fe impurity was found to be beneficial for mechanical property enhancement in the LPBFed samples. The parameters including the combination of laser power of 200 W, scanning speed of 1110 mm/s, hatch spacing of 0.15 mm, layer thickness of 0.03 mm and laser volumetric energy density of 40 J/mm^3 were optimized to achieve a high relative density of 99.7%. The as-LPBFed AlSi12FeMn alloy was featured by a high density of significantly refined spherical α-Al(Fe,Mn)Si phase (10–50 nm), which was coherent with the Al matrix. Meanwhile, the as-LPBFed AlSi12FeMn alloy can deliver superior mechanical properties including the yield strength of 305 MPa, the ultimate tensile strength of 485 MPa and the fracture strain of 6.1%. The improved mechanical properties are attributed to synergistic strengthening mechanisms, including solid solution strengthening, grain boundary strengthening and precipitation strengthening. Moreover, the formation of high-density stacking faults (SFs) and Lomer-Cottrell locks (LCs) in localized regions can also offer strengthening in the as-LPBFed AlSi12FeMn alloy.

1. Introduction

Al–Si alloys near the eutectic composition are widely used as foundry alloys to make castings with complex shapes due to their excellent castability [1–3]. However, Al–Si alloys typically have coarse and acicular eutectic silicon in conventional castings [4], which is detrimental to the mechanical properties. Traditionally, the approaches to improve the mechanical properties of Al–Si foundry alloys include the addition of refiners of AlTiB to refine primary Al phase and modifiers of Sr and Na to refine eutectic Si phase, the manufacturing of castings under high cooling rates [5,6], and the addition of strenghtening elements such as Mg, Zn, Cu et al. [7,8]. The

* Corresponding author.
** Corresponding author.
E-mail addresses: Xixi.Dong@brunel.ac.uk (X. Dong), y-hailin@csu.edu.cn (H. Yang).
https://doi.org/10.1016/j.jmrt.2022.04.008

high cooling rate can result in microstructural refinement and solute enhancement in solid solution. The higher the cooling rates, the signifier the enhancement in mechanical properties can be achieved [9–11]. However, the cooling rate is limited by the mould materials and the wall thickness of castings, in which the cooling rates in thin-wall die castings can be up to 10^3 K/s, but that in extra thick casting is much less than 10^{-2} K/s in conventional casting techniques [12,13].

One of the significant concerns in Al–Si foundry alloys is the existence of impurity Fe, which can easily form long and needle shaped β-AlFeSi phase. Generally, β-AlFeSi phase is detrimental to the mechanical properties and heat treatment can not significantly alter the morphology of Fe-containing phases. The Mn is usually added to neutralise Fe to induce the transformation from β-AlFeSi to the blocky and compact α-Al(Fe,Mn)Si that is relatively less detrimental to the mechanical properties [14]. It was reported [15] that the generation of α-Al(Fe,Mn)Si phase in the high Fe-containing Al–Mg–Si alloys by modulating the ratio of Mn and Fe can improve the yield strength [16]. Although the addition of Mn can reduce the detrimental effect of Fe, the Fe-containing intermetallic compounds still show irregular shapes and relatively large size due to the relatively low cooling rates during casting [17]. Therefore, it is significant to refine Fe-containing compounds in the Al–Si alloys with high Fe contents. It is not only beneficial for mechanical property improvement, but also important to use recycled materials in industry reduce the energy consumption and carbon foot print in final products.

Laser powder bed fusion (LPBF) is one of the metal additive manufacturing (AM) technologies to make parts with complex geometries and to achieve ultrafine microstructures through rapid solidification [18–20]. Because of its unique characteristics, LPBF has received increasingly considerable attention in a wide range of metallic materials such as aluminum alloys [21], copper alloys [22], steel [23], magnesium alloys [24], titanium alloys [25] and nickel alloys [26]. Due to the excellent castability and low shrinkage, the Al–12Si alloys have excellent capability of LPBF process [21]. Although previous studies have focused on the effects of different LPBF process parameters including atmosphere [27], hatch styles [28], build orientation [29] on the microstructure and mechanical properties of AlSi12 alloys. However, the reported mechanical properties of as-LPBFed AlSi12 alloy are relatively mediocre. The information for the effect of impurity Fe on the microstructure and mechanical properties of as-LPBFed AlSi12 alloys was very limited.

In this study, we present the effect of LPBF on the microstructure and mechanical properties of AlSi12 based alloys with high Fe content. An AlSi12FeMn alloy was investigated from the optimization of LPBF process parameters to the strengthening mechanism. In particular, the effect of α-Al(Fe,Mn)Si intermetallic on the strengthening is examined and discussed in the experimental alloys.

2. Experimental

The AlSi12FeMn powder was produced by argon gas atomization. The particle sizes of the powder were measured in terms of a laser particle size analyser (Mastersizer 3000, Malvern). The chemical composition of the powder was determined by inductively coupled plasma atomic emission spectrometry (ICP-OES, ICAP7000 Series, Thermo scientific) and the results are shown in Table 1. The LPBF system equipped with an IPG laser (FS271M, Farsoon) was used to fabricate the cubic samples with the dimension of $10 \times 10 \times 10$ mm^3 and the dog-bone shaped tensile samples with a gauge length of 30 mm, as shown in Figs. 1a andb and . The scanning strategy of the laser beam is schematically shown in Fig. 1c, in which laser scanning was rotated 67° layer-by-layer. The processing parameters are as follows: laser power at 200 W, scanning speeds between 555 and 2200 mm/s, layer thickness at 0.03 mm, hatch spacing at 0.15 mm and base plate heating to 373 K. Pure argon was used to purge the chamber during processing in order to avoid oxidation of samples.

The relative density of the as-fabricated samples was evaluated by the Archimedes principle. Structural analysis was performed by X-ray diffraction (XRD) from a Rigaku X-2000 with Cu-K_α radiation ($\lambda_{k\alpha} = 1.54$ Å) at 40 kV. The microstructural features were observed by an FEI Helios NanoLab G3 UC scanning electron microscopy (SEM) equipped with an energy dispersive X-ray spectrometer (EDS). The samples were mechanically polished and etched with Keller's reagent before SEM examination. Electron back scattered diffraction (EBSD) was conducted on ion polished sample in the same SEM equipped with a Hikari camera and the TSL OIM data analysis software. Detailed microstructure was further analyzed using transmission electron microscopy (TEM, Tecnai G2 F20). Thin foil samples for the TEM analysis were prepared by precision ion polishing system (PIPS).

For the mechanical test samples, both sides of the as-LPBFed samples were mechanically ground using the 2000 grit SiC papers, followed by polishing to required surface quality. According to ISO standard 6892, the uniaxial tensile tests were performed at room temperature by MTS Alliance RT30 tensile testing machine under the strain rate of 1×10^{-3} s^{-1}. Micro-hardness measurement was carried out using a Buehler 5104 micro-Vickers hardness tester with a load of 200 g for 15 s. The reported data are the average value of at least 5 measurements.

3. Results and discussion

The morphology of the powder particles is shown in Fig. 2. The powder particles were spheroidal with few small satellite particles attached to the big powder particles, as shown in Fig. 2a. The particle sizes of the powder were distributed from 9.9 to 58.8 μm with the median size of 31.5 μm (Fig. 2b).

The effects of laser volumetric energy density (ED_V) on the density and hardness of the AlSi12FeMn alloy are shown in

Table 1 – The chemical composition of experimental alloy powder.

Alloy(wt.%)	Si	Fe	Mn	Mg	Others	Al
AlSi12FeMn	11.25	0.54	0.26	0.01	<0.03	Bal.

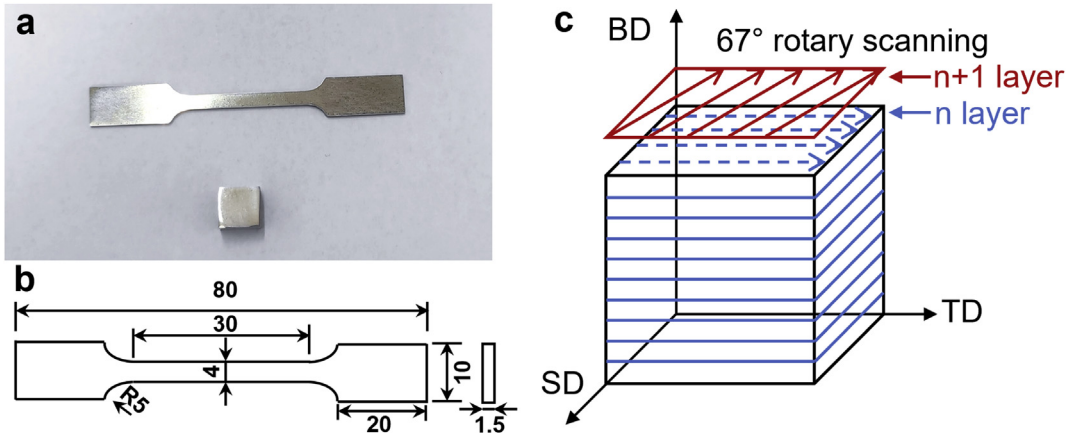

Fig. 1 – (a) Optical micrograph (OM) of the AlSi12FeMn samples; (b) Sample size for tensile test; (c) Schematic of the scanning strategy between successive layers in the LPBF process.

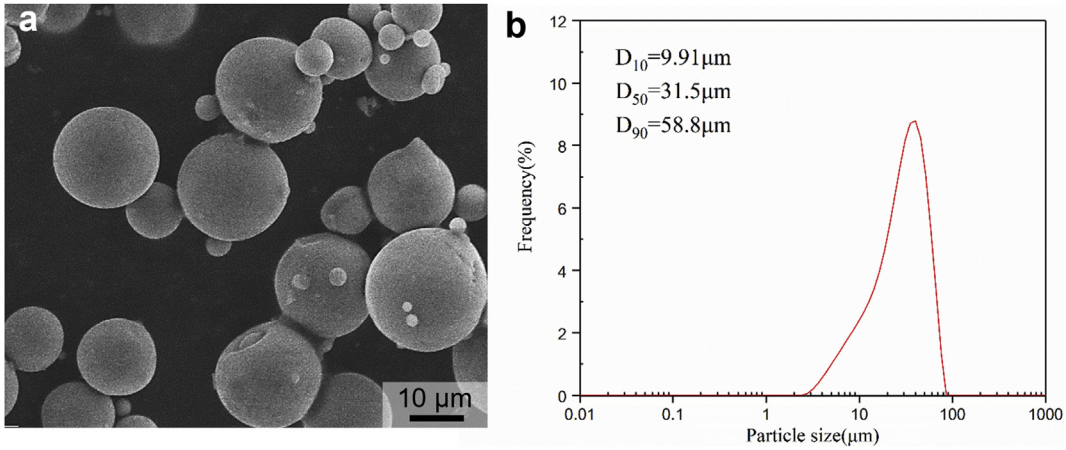

Fig. 2 – (a) SEM micrograph showing the morphology of the AlSi12FeMn alloy powder; (b) The distribution of particle size in the powder.

Fig. 3. The laser volume energy density under the processing parameters could be expressed by [21,30]: $ED_V=P/(Vht)$, where V is the scanning speed (mm/s), h is the hatch spacing (mm), t is the layer thickness (mm) and P is the laser power (W). From Fig. 3a, with the increase of the laser energy density, the relative density increased quickly to achieve the peak and then decreased slowly. The highest relative density was ~99.7% at ED_V = 40 J/mm^3. The relative density was very low when ED_V < 30 J/mm^3, which can be attributed to the insufficient laser energy to completely melt the powders and poor

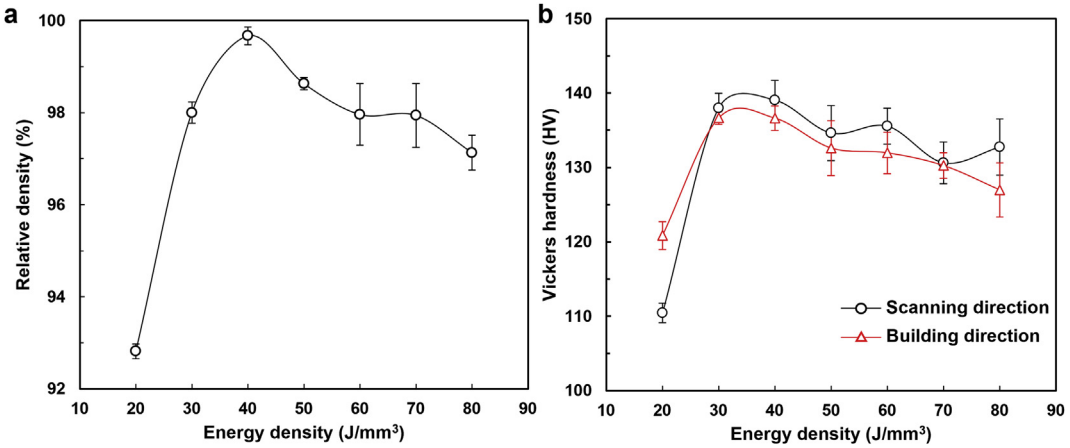

Fig. 3 – The effects of laser energy density on (a) the relative density and (b) the hardness of the as-LPBFed AlSi12FeMn alloy.

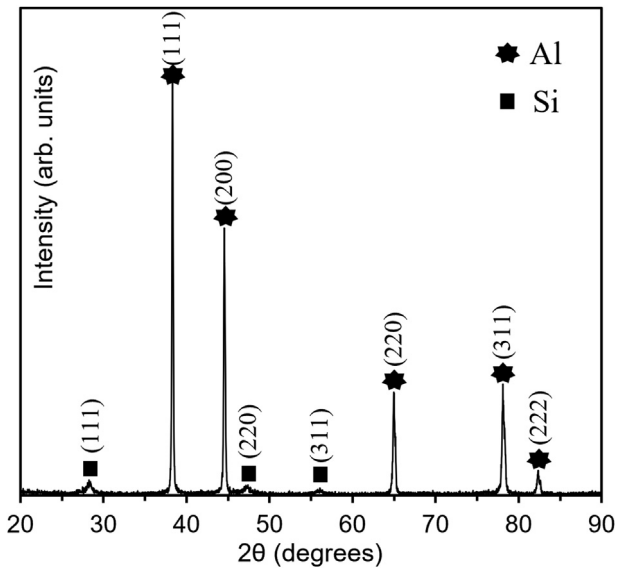

Fig. 4 – XRD patterns of the as-LPBFed AlSi12FeMn alloy.

metallurgical bonding between the solidified layers [31]. When the laser energy density was excessively high, the energetic arc resulted in turbulence flow in the melt pool and led to the formation of porosity and other defects [32]. Similar trends could be obtained for the hardness of the as-fabricated samples, as shown in Fig. 3b. The trend of hardness was correspondingly similar to that of the relative density. Only a little difference was observed for the hardness obtained in the scanning and building directions. The peak hardness was achieved at 139 Hv in the scanning direction and 136 Hv in the building direction when ED_V was 40 J/mm^3. According to the above analysis, the optimized LPBF process parameters were $P = 200$ W, $V = 1110$ mm/s, $h = 0.15$ mm, $t = 0.03$ mm and $ED_V = 40$ J/mm^3.

The XRD pattern in Fig. 4a revealed the phases formed in the as-LPBFed AlSi12FeMn alloy. It is clear that Al and Si phases existed in the alloy. No Fe-containing and Mn-containing phases were detected in Fig. 4, which may be due to the small amount of the Fe-containing and Mn-containing phases that could not be detected by XRD. In some cases, however, the dissolution of the substrate in suitable acid and separation of precipitates is an effective method for studying precipitates with very low percentage [33]. SEM images for the microstructure of the as-LPBFed AlSi12FeMn alloy along the scanning direction and the building direction are shown in Figs. 5a and b, respectively. It was observed that the typical melt pool (MP) microstructure consisted of MP coarse zone, MP fine zone and heat affected zone (HAZ) boundaries. The continuous network of Si-rich eutectic structure was present in both directions. However, more equiaxed grains were found in the scanning direction and more columnar grains were observed in the building direction. In addition, the cellular Al matrix was surrounded by spherical eutectic Si particles with the diameter of ~ 100–200 nm. Similar microstructures have been reported in as-LPBFed Al–Si alloys [18,29,34].

The results of the inverse pole figure (IPF) orientation maps are shown in Fig. 6 for the grain boundaries obtained by EBSD on the scanning and building direction in the as-LPBFed AlSi12FeMn alloy. Only equiaxed grains can be seen in the scanning direction (Fig. 6a). The characteristics of melt pool were easily distinguished by the clear coarse grains zone and fine grains zone. The microstructure in the building direction was mainly composed of columnar grains and some equiaxed grains (Fig. 6b). Similar to the scanning direction, the melt pool boundaries were also obviously observed in the building direction due to the presence of fine equiaxed grains at the end of the columnar grains. The average grain size in both directions was similar, which was 11.03 μm and 12.67 μm in the scanning direction and building direction, respectively. According to the Hall–Patch relationship, it is known that the fine grains are significantly beneficial to the strength improvement of the alloy [30].

To further confirm the phase structure and strengthening mechanism of the as-LPBFed AlSi12FeMn alloy, the detailed

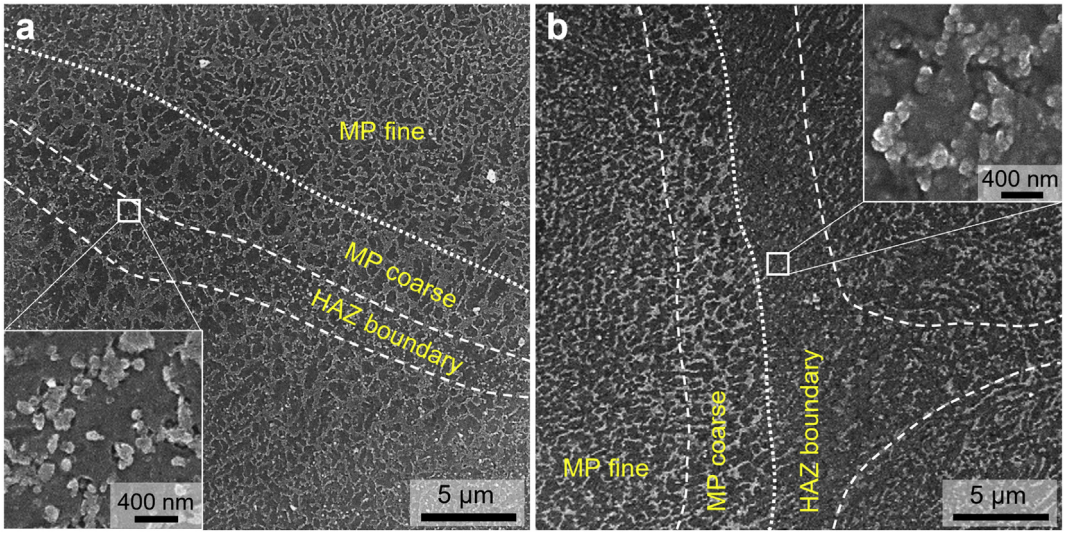

Fig. 5 – (a) SEM micrograph in scanning direction and (b) SEM micrograph in building direction (insert: high magnification at the white frame area).

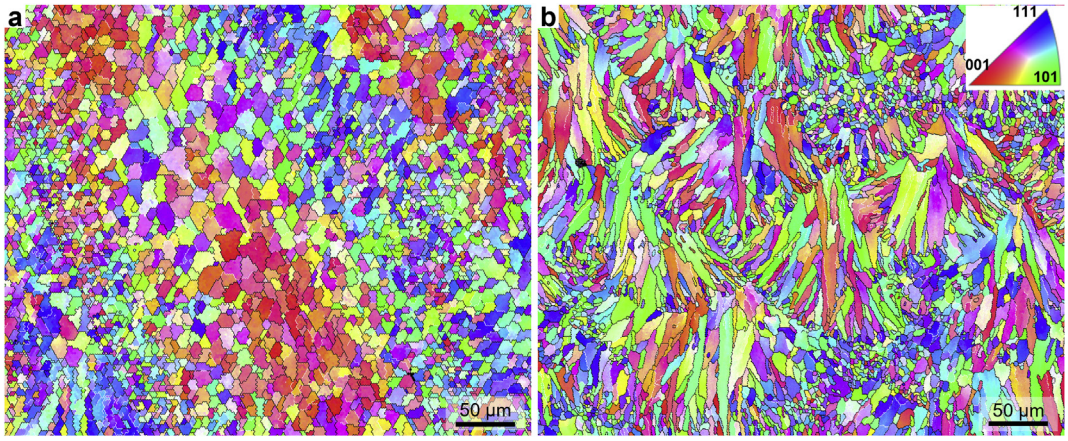

Fig. 6 – IPF orientation mapping images obtained by EBSD showing the microstructural features of as-LPBFed AlSi12FeMn alloy in (a) scanning direction and (b) building direction.

TEM investigations were conducted. The bright-field TEM image in Fig. 7a showed the submicron spherical particles surrounding the cell-like sub-structure. Fig. 7b and c shows the typical high-resolution TEM (HRTEM) image of the precipitate in the as-LPBFed AlSi12FeMn alloy and its corresponding fast Fourier transform (FFT). It can be seen that the interface of Al/precipitate had a good orientation relationship and the atoms could be fully coherent with each other. In order to clearly analyse the elements of the precipitated phase, the HADDF-STEM image of the cellular structure and the corresponding EDS mapping are shown in Fig. 7d. The results further proved that the precipitates were α-Al(Fe,Mn)Si and the presence of residual Si particles. The Si particles were compact with a diameter of about 100–200 nm, which were consistent with the results observed in the SEM micrograph. More importantly, the dimension of α-Al(Fe,Mn)Si phase was about 10–50 nm, which indicates that the α-Al(Fe,Mn)Si phase was greatly refined by the LPBF processing, in contrast to the conventional casting [35].

The high-density dislocations and the Orowan mechanism revealed that the nanometer α-Al(Fe,Mn)Si particles played a strong anchoring effect on the dislocations, as shown in Fig. 8a. In addition, the Si particles also had an obstructive effect on dislocations, which may be attributed to the semi-coherent interface between Si and Al phases [36]. Interestingly, Fig. 8b shows the formation of stacking faults (SFs) in

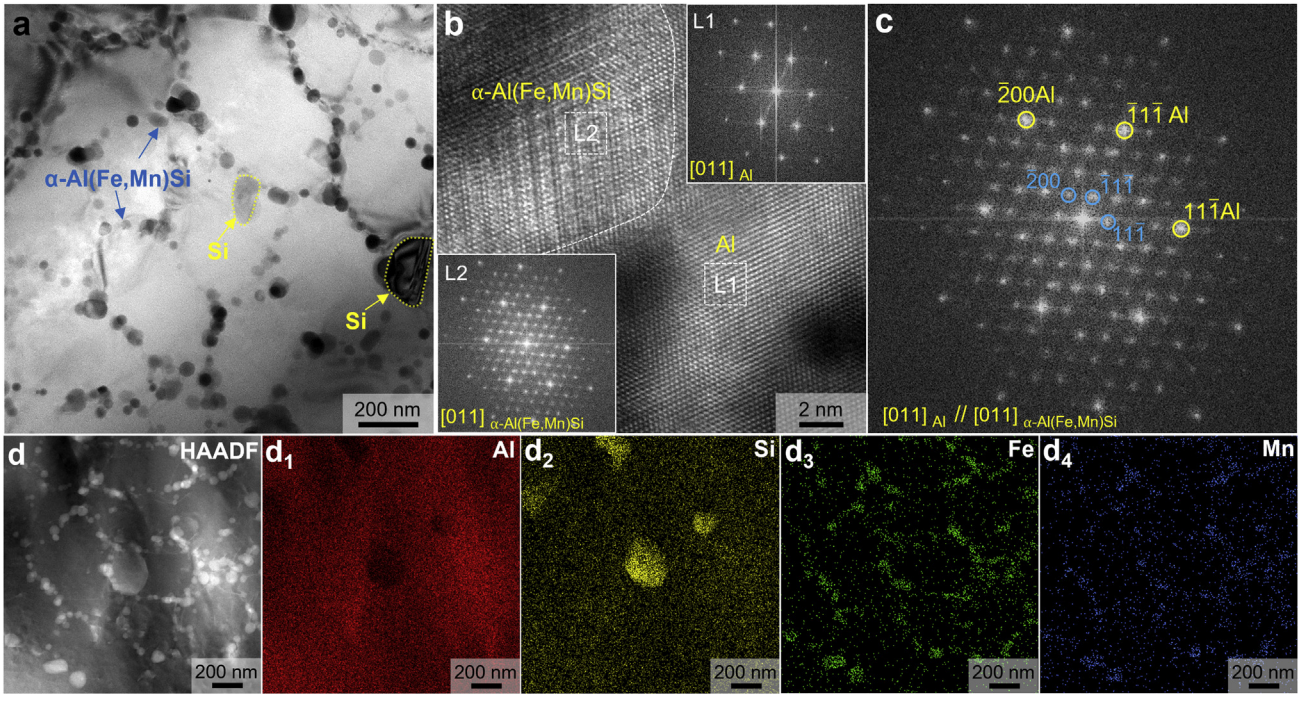

Fig. 7 – (a) Bright-field TEM showing the detailed microstructure in the as-LPBFed AlSi12FeMn alloy and (b) and (c) HRTEM image showing the interface of Al/α-Al(Fe,Mn)Si and inserts showing the orientation by FFT; (d, d_1-d_4) HADDF-STEM image of the cellular structure and the corresponding elemental mapping of Al, Si, Fe and Mn.

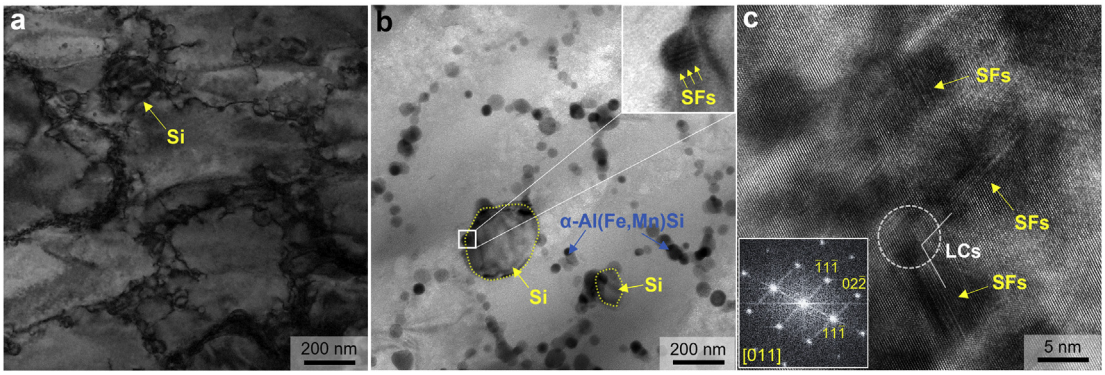

Fig. 8 – (a) Bright-field TEM image showing the interactions between nanoparticles and dislocations; (b) bright-field TEM image and (c) HRTEM image showing the formation of SFs and LCs, confirmed by the inserted inverse FFT pattern.

the Al matrix. The presence of high-density SFs and Lomer-Cottrell locks (LCs, formed by the intersection activities of the SFs) were confirmed through HRTEM image and its inverse FFT, as shown in Fig. 8c. The SFs are expected to distort the interfacial lattice and thus to impede the movement of dislocations in Al alloys [37]. In addition, similar to Orowan mechanism, LCs have the ability to accommodate dislocations and can anchor dislocations [38]. Normally, the existence of SFs in Al alloys is difficult because of the high stacking fault energy (SFE) of Al [39]. The presence of high-density SFs may be attributed to the supersaturated solid solution of Si in Al and the addition of Fe that decreases the SFE of Al alloys [40,41].

Obviously, α-Al(Fe,Mn)Si phases play a crucial role in improving the performance of the alloy. To analyse the forming process of α-Al(Fe,Mn)Si, the phase diagram of the Al–Si–Fe–Mn system was calculated with Pandat software and the results are shown in Fig. 9. According to the results, the α-Al phase precipitated from the melt first when the Fe content is < 0.25 wt.%; The primary phase is α-Al(Fe,Mn)Si phase when the Fe content is between 0.25 and 1.13 wt.%; And the β-AlFeSi phase precipitated first when the Fe content is > 1.13 wt.%. In the present study, the Fe content of the AlSi12FeMn alloy is 0.53 wt.%. The α-Al(Fe,Mn)Si phase precipitated first from the melt at 878 K, followed by the α-Al phase, β-AlFeSi phase and Si phase in sequential order. This is another proof that the α-Al(Fe,Mn)Si phase can be formed in the as-LPBFed AlSi12FeMn alloy.

The tensile properties of the as-LPBFed AlSi12FeMn alloy prepared using the optimized parameters are shown in Fig. 10a. The yield strength (YS), ultimate tensile strength (UTS) and fracture strain of the as-LPBFed samples are 305 ± 5 MPa, 485 ± 8 MPa and 6.1 ± 0.3%, respectively. The comparison of mechanical properties from the present study and from the literatures for Al–Si based alloys with high Si content is shown in Fig. 10b. Clearly, the as-LPBFed AlSi12-FeMn alloy exhibits excellent strength and ductility among other Al–Si alloys including AlSi12 alloys [18,27–29,42–47]

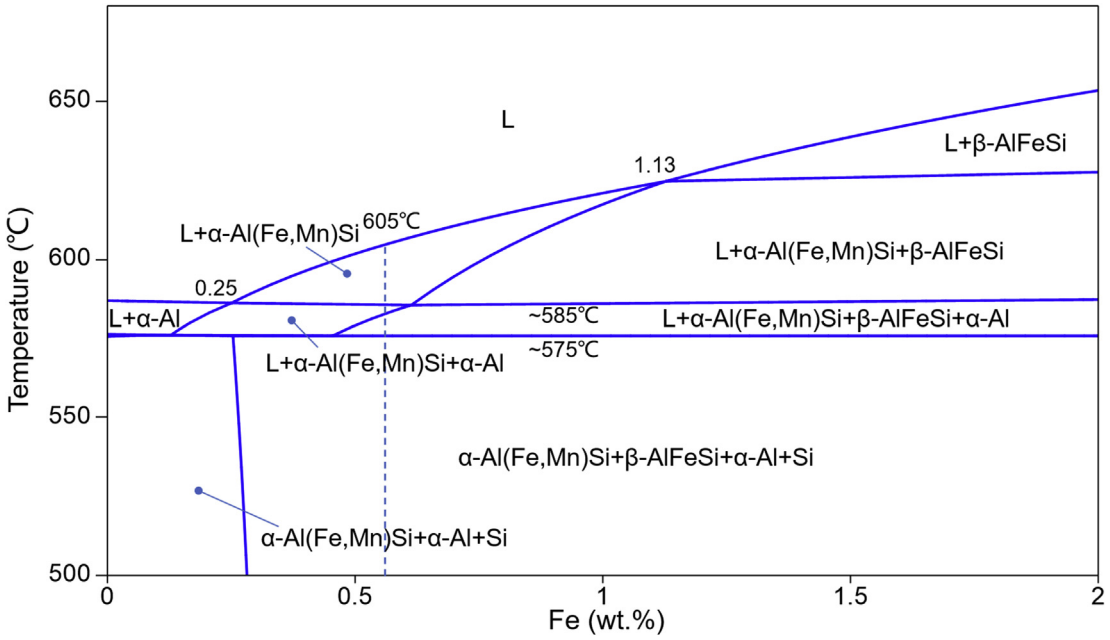

Fig. 9 – Phase diagram of AlSi12FeMn alloy with varying Fe content calculated by the PANDAT software.

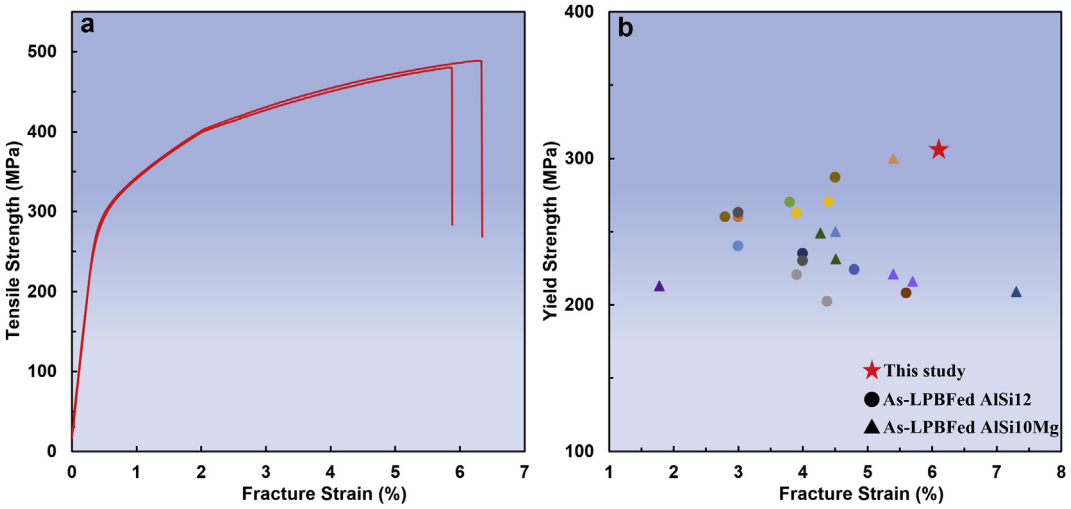

Fig. 10 – (a) Typical tensile stress–strain curves of as-LPBFed AlSi12FeMn alloy and (b) the comparison of the tensile properties of the as-LPBFed AlSi12FeMn alloy with the reference as-LPBFed AlSi12 and AlSi10Mg alloys.

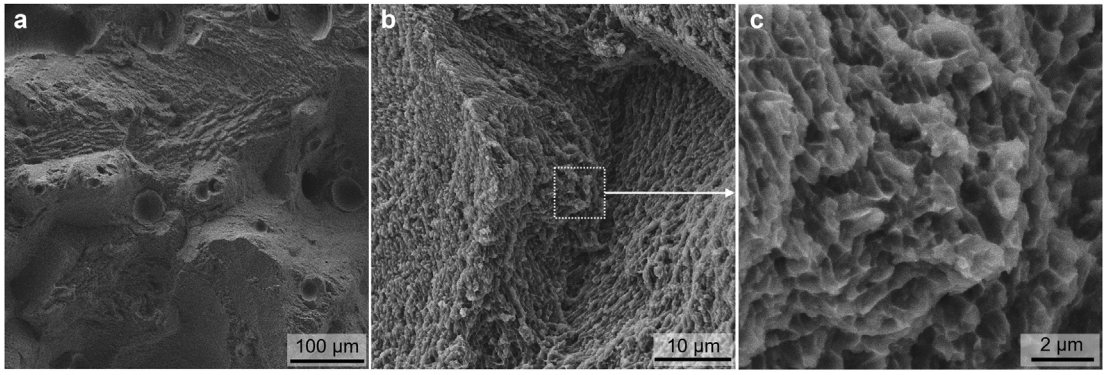

Fig. 11 – (a) Fracture surface of the as-LPBFed AlSi12FeMn alloys and (b–c) high magnifications.

and AlSi10Mg alloys [34,48–52]. The average yield strength and fracture strain of the as-LPBFed AlSi12 alloys in literatures are ~245 MPa and ~3.9%. In this study, the yield strength and ductility were increased by ~60 MPa and ~2.2%, respectively.

Fig. 11 shows the fracture surface of the tensile samples. It can be observed that the existence of a step-like morphology and ripple patterns near pores are followed by flatter areas. It indicates that the crack initiated from porous area and propagated rapidly after plastic deformation to some extent. The formation of pores cannot be completely prevented and they are the most common defect in the LPBF processing due to the un-melted powder or the presence of moisture on the surfaces of the powder [21]. The features of ductile fracture with numerous tear ridges accompanied by dimples can be seen in Figs. 11b and c.

Generally, the high strength mainly comes from multiple strengthening mechanisms, including solid solution strengthening, nano-sized α-Al(Fe,Mn)Si phase, SFs and LCs. In the LPBF condition, the solid solubility of Si in the Al matrix can reach ~ 7 wt% to 8 wt% instead of the expected 1.6 wt% [18,53], which will enhance the strength of the as-LPBFed AlSi12FeMn alloy. In contrast to the die-casting condition where the size of the α-Al(Fe,Mn)Si phase is ~ 1 μm [35], the α-Al(Fe,Mn)Si phase is dramatically refined under as-LPBFed condition. The cooling rate during the fabricated process is a critical factor, which is 500–1000 K/s in die-casting but ~ 10^4–10^6 K/s in LPBF process. The high cooling rate leads to the significant refinement of the α-Al(Fe,Mn)Si phase to size of 10–50 nm. More importantly, the interface of α-Al(Fe,Mn)Si phase and α-Al phase has a good coherent relationship. On the other hand, the formation of SFs in Al alloys has been reported as well [18,36,54]. The strengthening effect of SFs and LCs phases on mechanical properties has been discussed previously. Therefore, the SFs and LCs phases and the precipitation strengthening from the α-Al(Fe,Mn)Si phase contributed the dominant effect in the strength improvement.

4. Conclusions

In this work, we processed a high Fe-containing AlSi12FeMn alloy by LPBF. The fabricated alloy samples have demonstrated excellent mechanical properties. The key findings can be drawn as follows:

(1) A high relative density of 99.7% for as-LPBFed AlSi12-FeMn alloy was obtained by the optimized parameters of LPBF process as follow: laser power of 200 W, scanning speed of 1110 mm/s, hatch spacing of 0.15 mm,

layer thickness of 0.03 mm and laser volumetric energy density of 40 J/mm^3.

(2) The as-LPBFed AlSi12FeMn alloy could offer superior mechanical properties including the yield strength of 305 MPa, the ultimate tensile strength of 485 MPa and the fracture strain of 6.1%. The improved mechanical properties were attributed to synergistic strengthening of solid solution, grain boundary and precipitation. Furthermore, the formation of high-density SFs and LCs in localised regions could also offer strengthening in the as-LPBFed AlSi12FeMn alloy.

(3) The as-LPBFed AlSi12FeMn alloy was featured by significantly refined compact α-Al(Fe,Mn)Si phase with a size of 10–50 nm. The α-Al(Fe,Mn)Si phase was coherent with the α-Al phase in the interface.

(4) The high-density SFs and LCs were formed in the as-LPBFed AlSi12FeMn alloy, which were ~5 nm in size and normally located near the α-Al(Fe,Mn)Si phases. Meanwhile, the high-density SFs and LCs were found to be beneficial for the strengthening of the as-LPBFed AlSi12FeMn alloy.

Declaration of Competing Interest

The authors declare that they have no known competing financial interests or personal relationships that could have appeared to influence the work reported in this paper.

Acknowledgement

Financial support from the National Key Research and Development Program of China, China (Grant No. 2020YFB0311300ZL), National Natural Science Foundation of China, China (Grant No. 52071343), and supported by the Fundamental Research Funds for the Central Universities of Central South University, China; Postgraduate Scientific Research Innovation Project of Hunan Province, China are gratefully acknowledged.

REFERENCES

[1] Miller WS, Zhuang L, Bottema J, Wittebrood AJ, De Smet P, Haszler A, et al. Recent development in aluminium alloys for the automotive industry. Mater Sci Eng, A 2000;280:37–49.
[2] Reddy AP, Krishna PV, Rao RN, Murthy NV. Silicon carbide reinforced aluminium metal matrix nano composites-A review. Mater Today Proc 2017;4:3959–71.
[3] Azadi M, Bahmanabadi H, Gruen F, Winter G. Evaluation of tensile and low-cycle fatigue properties at elevated temperatures in piston aluminum-silicon alloys with and without nano-clay-particles and heat treatment. Mater Sci Eng, A 2020;788:139497.
[4] McDonald SD, Nogita K, Dahle AK. Eutectic nucleation in Al–Si alloys. Acta Mater 2004;52:4273–80.
[5] Dinnis CM, Taylor JA, Dahle AK. As-cast morphology of iron-intermetallics in Al–Si foundry alloys. Scripta Mater 2005;53:955–8.
[6] Yi JZ, Gao YX, Lee PD, Lindley TC. Effect of Fe-content on fatigue crack initiation and propagation in a cast aluminum–silicon alloy (A356–T6). Mater Sci Eng, A 2004;386:396–407.
[7] Zhang M, Liu K, Han J, Qian F, Wang J, Guan S. Investigating the role of Cu, Zr and V on the evolution of microstructure and properties of Al-Si-Mg cast alloys. Mater Today Commun 2021;26:102055.
[8] Wang D, Liu S, Zhang X, Li X, Zhang H, Nagaumi H. Fast aging strengthening by hybrid precipitates in high pressure die-cast Al-Si-Cu-Mg-Zn alloy. Mater Charact 2021;179:111312.
[9] Liu R, Zheng J, Godlewski L, Zindel J, Li M, Li W, et al. Influence of pore characteristics and eutectic particles on the tensile properties of Al–Si–Mn–Mg high pressure die casting alloy. Mater Sci Eng, A 2020;783:139280.
[10] Yoon SC, Hong SJ, Hong SI, Kim HS. Mechanical properties of equal channel angular pressed powder extrudates of a rapidly solidified hypereutectic Al-20wt% Si alloy. Mater Sci Eng, A 2007;449:966–70. -51.
[11] Dasgupta R. Property improvement in Al–Si alloys through rapid solidification processing. J Mater Process Technol 1997;72:380–4.
[12] Yang WC, Yang XL, Ji SX. Melt superheating on the microstructure and mechanical properties of diecast Al-Mg-Si-Mn alloy. Met Mater Int 2015;21:382–90.
[13] Ji SX, Wang Y, Watson D, Fan Z. Microstructural evolution and solidification behavior of Al-Mg-Si alloy in high-pressure die casting. Metall Mater Trans A 2013;44:3185–97.
[14] Kuijpers NCW, Vermolen FJ, Vuik C, Koenis PTG, Nilsen KE, Zwaag SVD. The dependence of the β-AlFeSi to α-Al(FeMn)Si transformation kinetics in Al–Mg–Si alloys on the alloying elements. Mater Sci Eng, A 2005;394:9–19.
[15] Wang Y, Deng Y, Dai Q, Jiang K, Chen J, Guo X. Microstructures and strengthening mechanisms of high Fe containing Al–Mg–Si–Mn–Fe alloys with Mg, Si and Mn modified. Mater Sci Eng, A 2021;803:140477.
[16] Ji SX, Yang WC, Gao F, Watson D, Fan ZY. Effect of iron on the microstructure and mechanical property of Al–Mg–Si–Mn and Al–Mg–Si diecast alloys. Mater Sci Eng, A 2013;564:130–9.
[17] Rakhmonov J, Liu K, Rometsch P, Parson N, Chen XG. Effects of Al(MnFe)Si dispersoids with different sizes and number densities on microstructure and ambient/elevated-temperature mechanical properties of extruded Al–Mg–Si AA6082 alloys with varying Mn content. J Alloys Compd 2021;861:157937.
[18] Li XP, Wang XJ, Saunders M, Suvorova A, Zhang LC, Liu YJ, et al. A selective laser melting and solution heat treatment refined Al–12Si alloy with a controllable ultrafine eutectic microstructure and 25% tensile ductility. Acta Mater 2015;95:74–82.
[19] Prashanth KG, Eckert J. Formation of metastable cellular microstructures in selective laser melted alloys. J Alloys Compd 2017;707:27–34.
[20] Wu J, Wang XQ, Wang W, Attallah MM, Loretto MH. Microstructure and strength of selectively laser melted AlSi10Mg. Acta Mater 2016;117:311–20.
[21] Aboulkhair NT, Simonelli M, Parry L, Ashcroft I, Tuck C, Hague R. 3D printing of Aluminium alloys: additive Manufacturing of Aluminium alloys using selective laser melting. Prog Mater Sci 2019;106:100578.
[22] Ren Z, Zhang DZ, Fu G, Jiang J, Zhao M. High-fidelity modelling of selective laser melting copper alloy: laser reflection behavior and thermal-fluid dynamics. Mater Des 2021;207:109857.
[23] Saxena P, Gajera H, Shah D, Pancholi N. Effect of SLM process parameters on hardness and microstructure of stainless steel 316 material. Mater Today Proc 2022;50:1653–9.
[24] Zhang WN, Wang LZ, Feng ZX, Chen YM. Research progress on selective laser melting (SLM) of magnesium alloys: a review. Optik 2020;207:163842.

[25] Singh N, Hameed P, Ummethala R, Manivasagam G, Prashanth KG, Eckert J. Selective laser manufacturing of Ti-based alloys and composites: impact of process parameters, application trends, and future prospects. Mater Today Adv 2020;8:100097.
[26] Leary M, Mazur M, Williams H, Yang E, Alghamdi A, Lozanovski B, et al. Inconel 625 lattice structures manufactured by selective laser melting (SLM): mechanical properties, deformation and failure modes. Mater Des 2018;157:179–99.
[27] Wang XJ, Zhang LC, Fang MH, Sercombe TB. The effect of atmosphere on the structure and properties of a selective laser melted Al–12Si alloy. Mater Sci Eng, A 2014;597:370–5.
[28] Prashanth KG, Scudino S, Eckert J. Defining the tensile properties of Al-12Si parts produced by selective laser melting. Acta Mater 2017;126:25–35.
[29] Rashid R, Masood SH, Ruan D, Palanisamy S, Rahman RRA, Elambasseril J, et al. Effect of energy per layer on the anisotropy of selective laser melted AlSi12 aluminium alloy. Addit Manuf 2018;22:426–39.
[30] Yang HL, Zhang YY, Wang JY, Liu ZL, Liu CH, Ji SX. Additive manufacturing of a high strength Al-5Mg2Si-2Mg alloy: microstructure and mechanical properties. J Mater Sci Technol 2021;91:215–23.
[31] Zhang J, Song B, Wei Q, Bourell D, Shi Y. A review of selective laser melting of aluminum alloys: processing, microstructure, property and developing trends. J Mater Sci Technol 2019;35:270–84.
[32] Shi X, Ma S, Liu C, Wu Q. Parameter optimization for Ti-47Al-2Cr-2Nb in selective laser melting based on geometric characteristics of single scan tracks. Opt Laser Technol 2017;90:71–9.
[33] Khalaj G, Yoozbashizadeh H, Khodabandeh A, Tamizifar M. Austenite grain growth modelling in weld heat affected zone of Nb/Ti microalloyed linepipe steel. Mater Sci Technol 2014;30:424–33.
[34] Chen B, Moon SK, Yao X, Bi G, Shen J, Umeda J, et al. Strength and strain hardening of a selective laser melted AlSi10Mg alloy. Scripta Mater 2017;141:45–9.
[35] Dong X, Youssef H, Zhu X, Zhang Y, Wang S, Ji S. High as-cast strength die-cast AlSi9Cu2Mg alloy prepared by nanoparticle strengthening with industrially acceptable ductility. J Alloys Compd 2021;852:156873.
[36] Miao Q, Wu D, Chai D, Zhan Y, Bi G, Niu F, et al. Comparative study of microstructure evaluation and mechanical properties of 4043 aluminum alloy fabricated by wire-based additive manufacturing. Mater Des 2020;186:108205.
[37] Li R, Wang M, Li Z, Cao P, Yuan T, Zhu H. Developing a high-strength Al-Mg-Si-Sc-Zr alloy for selective laser melting: crack-inhibiting and multiple strengthening mechanisms. Acta Mater 2020;193:83–98.
[38] Wang J, Yang H, Huang H, Zou J, Ji S, Liu Z. High strength-ductility Co23Cr23Ni23Mn31 medium-entropy alloy achieved via defect engineering. Mater Sci Eng, A 2020;796:139974.
[39] Swygenhoven HV, Derlet PM, Frøseth AG. Stacking fault energies and slip in nanocrystalline metals. Nat Mater 2004;3:399–403.
[40] Suzuki H. Segregation of solute atoms to stacking faults. J Phys Soc Jpn 1962;17:322–5.
[41] Li Q, Cho J, Xue S, Sun X, Zhang Y, Shang Z, et al. High temperature thermal and mechanical stability of high-strength nanotwinned Al alloys. Acta Mater 2019;165:142–52.
[42] Prashanth KG, Scudino S, Eckert J. Tensile properties of Al-12Si fabricated via selective laser melting (SLM) at different temperatures. Technologies 2016;4:38.
[43] Hosseinzadeh A, Radi A, Richter J, Wegener T, Sajadifar SV, Niendorf T, et al. Severe plastic deformation as a processing tool for strengthening of additive manufactured alloys. J Manuf Process 2021;68:788–95.
[44] Prashanth KG, Scudino S, Klauss HJ, Surreddi KB, Löber L, Wang Z, et al. Microstructure and mechanical properties of Al–12Si produced by selective laser melting: effect of heat treatment. Mater Sci Eng, A 2014;590:153–60.
[45] Siddique S, Imran M, Wycisk E, Emmelmann C, Walther F. Influence of process-induced microstructure and imperfections on mechanical properties of AlSi12 processed by selective laser melting. J Mater Process Technol 2015;221:205–13.
[46] Suryawanshi J, Prashanth KG, Scudino S, Eckert J, Prakash O, Ramamurty U. Simultaneous enhancements of strength and toughness in an Al-12Si alloy synthesized using selective laser melting. Acta Mater 2016;115:285–94.
[47] Wang P, Lao CS, Chen ZW, Liu YK, Wang H, Wendrock H, et al. Microstructure and mechanical properties of Al-12Si and Al-3.5Cu-1.5Mg-1Si bimetal fabricated by selective laser melting. J Mater Sci Technol 2020;36:18–26.
[48] Martin JH, Yahata BD, Hundley JM, Mayer JA, Schaedler TA, Pollock TM. 3D printing of high-strength aluminium alloys. Nature 2017;549:365–9.
[49] Patakham U, Palasay A, Wila P, Tongsri R. MPB characteristics and Si morphologies on mechanical properties and fracture behavior of SLM AlSi10Mg. Mater Sci Eng, A 2021;821:141602.
[50] Tradowsky U, White J, Ward RM, Read N, Reimers W, Attallah MM. Selective laser melting of AlSi10Mg: influence of post-processing on the microstructural and tensile properties development. Mater Des 2016;105:212–22.
[51] Ben DD, Ma YR, Yang HJ, Meng LX, Shao XH, Liu HQ, et al. Heterogeneous microstructure and voids dependence of tensile deformation in a selective laser melted AlSi10Mg alloy. Mater Sci Eng, A 2020;798:140109.
[52] Delahaye J, Tchuindjang JT, Lecomte-Beckers J, Rigo O, Habraken AM, Mertens A. Influence of Si precipitates on fracture mechanisms of AlSi10Mg parts processed by Selective Laser Melting. Acta Mater 2019;175:160–70.
[53] Li W, Li S, Liu J, Zhang A, Zhou Y, Wei Q, et al. Effect of heat treatment on AlSi10Mg alloy fabricated by selective laser melting: microstructure evolution, mechanical properties and fracture mechanism. Mater Sci Eng, A 2016;663:116–25.
[54] Wang M, Knezevic M, Gao H, Wang J, Kang M, Sun B. Phase interface induced stacking faults in Al-7.5Y alloy revealed by in-situ synchrotron X-ray diffraction and ex-situ electron microscopy. Mater Charact 2021;179:111322.